New Scheme for Impervious Surface Area Mapping From SAR Images With Auxiliary User-Generated Content

Wen Wu, Zelang Miao, *Member, IEEE*, Yuelong Xiao, Zhongbin Li, *Member, IEEE*, Anshu Zhang,
Alim Samat, *Member, IEEE*, Nianchun Du, Zhuokui Xu, and Paolo Gamba, *Fellow, IEEE*

***Abstract*—This article presents a new scheme to extract impervious surface area from synthetic-aperture radar (SAR) images exploiting auxiliary user-generated content (UGC). The presented scheme includes the automatic generation of training samples based on the combination of UGC and SAR data, and SAR data preprocessing, leading to impervious surface area classification through a clustering-based one-class support vector machine approach. Two areas—namely, the cities of Beijing and Taipei, have been analyzed using the Sentinel-1 SAR data to test and validate the proposed methodology. Experimental results show that the presented scheme improves the automatic selection of impervious surface training samples. Moreover, this scheme achieves a comparable classification performance to traditional methods without requiring time-consuming training point manual extraction. Results in this study will help to promote the application of UGC for urban remote sensing data interpretation.**

***Index Terms*—Clustering-based one-class support vector machine, impervious surface area (ISA), user-generated content (UGC), synthetic-aperture radar (SAR).**

I. Introduction

URBANIZATION is one of the most important socioeconomic phenomena in the world today. With the acceleration of global urbanization, a widespread conversion from natural to impervious surface area (ISA) has been observed, leading to considerable social and ecological consequences [1]. Accordingly, timely and accurate ISA products are essential for understanding several important issues, such as groundwater organic carbon change and rainfall management including flash flood effects in cities [2], [3]. The advent of modern remote sensing technologies provides rich data sources and enables monitoring of ISAs. In addition, several ISA maps exist with national to global coverage, including Urban Atlas [4], GlobeLand30 [5], and the Global Urban Footprint [6]. Recently, Gong *et al.* [7] generated annual maps of global artificial impervious areas from 1985 to 2018 using the archive of 30-m resolution Landsat images and other ancillary datasets (e.g., nighttime light data). Their results suggest that the global artificial impervious area has substantially expanded in the past three decades—the global artificial impervious area in 2018 was 1.5 times than that in 1990.

Multiple methods have been designed to estimate and map ISAs from different data sources (e.g., ground measurements or satellite images) to address the issue of accurate ISA mapping. Fieldwork and manual digitization of high-resolution remotely sensed data have long been utilized in terms of precise ISA mapping. Despite its great accuracy and robustness, this approach is labor-intensive and time-consuming; thus, mapping ISA at a regional/global scale is impossible [8]. The advent of modern technology has transformed ISA mapping from manual work to automated and/or semiautomated estimating and mapping imperviousness with the aid of image processing tools [9]. In the past two decades, several studies have been published on ISA extraction through multiple data sources and/or technologies [10]. Optical remotely sensed data and synthetic-aperture radar (SAR) are two typical data sources. Wang and Li [11] provided

Manuscript received July 3, 2020; revised September 7, 2020; accepted September 25, 2020. Date of publication September 29, 2020; date of current version October 12, 2020. This work was supported in part by the State Key Laboratory of Desert and Oasis Ecology, Xinjiang Institute of Ecology and Geography, Chinese Academy of Sciences under Grant G2019-02-06, in part by the National Natural Science Foundation of China under Grant 41701500, in part by the Natural Science Foundation of Hunan Province under Grant 2018JJ3641 and Grant 2019JJ60001, in part by the Scientific Research Fund of Hunan Provincial Education Department under Grant 13B129, in part by the Hong Kong RGC under Grant PolyU 152201/17E, in part by the Natural Science Foundation of Jiangsu Province under Grant BK20190785, in part by the Innovation-Driven Project of Central South University under Grant 2020CX036, in part by the Natural Science Foundation of Jiangsu Province under Grant BK20190785, and in part by the Postgraduate Innovation Project of Central South University under Grant 2020ZZTS693. *(Wen Wu, Zelang Miao, Yuelong Xiao, and Zhongbin Li contributed equally to this work.) (Corresponding author: Zelang Miao.)*

Wen Wu, Zelang Miao, and Yuelong Xiao are with the School of Geoscience and Info-Physics, Central South University, Changsha 410083, China, and also with the the Key Laboratory of Metallogenic Prediction of Nonferrous Metals and Geological Environment Monitoring, Central South University, Changsha 410083, China (e-mail: vennww@csu.edu.cn; zelang.miao@outlook.com; 1065021381@qq.com).

Zhongbin Li is with the Center for Global Change and Earth Observations, Michigan State University, East Lansing, MI 48823 USA (e-mail: lzbtongji@gmail.com).

Anshu Zhang is with the Department of Land Surveying and Geo-Informatics, The Hong Kong Polytechnic University, Kowloon, Hong Kong (e-mail: anshu.zhang@connect.polyu.hk).

Alim Samat is with the Xinjiang Institute of Ecology and Geography, Chinese Academy of Sciences, Xinjiang 830011, China (e-mail: alim.smt@gmail.com).

Nianchun Du is with the China Nonferrous Metal Changsha Survey and Design Institute Company, Ltd., Changsha 410000, China (e-mail: cegis@sina.com).

Zhuokui Xu is with the School of Traffic and Transportation Engineering, Changsha University of Science Technology, Changsha 410083, China (e-mail: 38783368@qq.com).

Paolo Gamba is with the Department of Industrial and Information Engineering, University of Pavia, 27100 Pavia, Italy (e-mail: paolo.gamba@unipv.it).

Digital Object Identifier 10.1109/JSTARS.2020.3027507

a comprehensive survey on impervious surface detection from remote sensing images. The mainstream ISA mapping from optical remotely sensed data includes the following: spectral mixing analysis [12], the exploitation of impervious surface indices [13], image classification methods [12], and multisource data fusion models [11]. Although numerous studies regard on delineating ISA from optical satellite images, the inherent characteristic of optical sensors still limits its application, for example, the cloud coverage does not allow obtaining an optical image with a satisfactory quality level in tropical areas [14]. To tackle these issues, ISA mapping from SAR has been introduced, either considering SAR data alone or SAR combined with optical images [15]. Compared with using only optical remotely sensed data, only a few studies directly investigate the application of SAR to ISA mapping, partly due to the lack of frequently efficient and worldwide available SAR images and partly because of the inadequacy of image processing algorithms suitable for SAR images [8]. The availability of free public accessibility to SAR data (e.g., Sentinel 1-A), the development of efficient image processing techniques, and enormous growth in computing power have recently lead to a renewed interest in ISA mapping from SAR.

On a different research line, the evolution and exponential growth of modern information technology (e.g., smart mobile devices, cloud computing, and Internet of Things) has expedited the availability of large amounts of data, the so-called big data [16]. The user-generated content (UGC) produced by people worldwide, either accidentally or intentionally, has proven to be an essential and cost-effective tool in a wide range of practical applications [17], [18]. This study uses the term UGC to sum up the broad-based and rich data sources contributed by various users of different backgrounds. Representative UGC includes, but is not limited to, social media data, volunteered geographic information (VGI), and publicly posted points of interest (POIs). Social media, generally referring to web applications allowing users to create, post, and share contents instantly [19], is an important UGC source. Although the percentage of social media users who are willing to share their geolocations is low [20], [21], the amount of geo-located social media data is still very large due to several social media users and relentlessly growing social media posts. In contrast to social media that generate geographic information unintentionally, VGI and POIs are routinely created by volunteers or third-party platforms (e.g., Google Maps) [22]. VGI [e.g., OpenStreetMap (OSM)] is a special kind of geospatial data contributed by worldwide volunteers with the aid of online public available mapping tools [23]– [25] and plays an essential role in UGC. Similar to VGI, POI is an emerging GIS terminology. A POI is a location that many people label as interesting or useful and which is significantly related to people's daily lives (e.g., a supermarket, a parking lot, a railroad station). Generally speaking, a POI consists of two parts—namely, the attribute (e.g., a name and a type) and the spatial information (e.g., the geographic coordinates) [26], [27], which are critical for various location-based services.

Current studies devoted to the use of UGC by the geo-informatics community are diverse, and many scholars have explored different potential information from UGC to meet their specific needs. For example, scholars have derived critical information from UGC for social science research, such as flu trends prediction, crime detection, and social sensing and economics [28]– [32]. Other works have focused on applications of UGC in the field of natural disasters, such as disaster reduction, emergency response, and humanitarian aid [33]–[38]. The geographic information is commonly associated with most instances of UGC and remotely sensed data. Hence, these two datasets can be co-registered, enabling the possibility to carry out a synergic geo-informatics study. For instance, VGI, real-estate locations obtained by Web Crawler, and geo-tagged photos have been taken as reference data to assess the accuracy of land cover/land use maps [39]–[42]. UGC and satellite images have been jointly used for land use/land cover mapping, road network generation and updating, labeling urban pixels, and collaborative mapping [43]–[45]. Some researchers have paid attention to uncertainty, data quality control, user privacy protection, and ethical issues of UGC [46]–[51]. Others have attempted to attach geographic tags to pictures/videos from unidentified sources based on street view images and 3-D reconstruction [52]–[54]. Although the last decade has seen a growing trend toward the integration of UGC and remotely sensed data [46], [55]–[58], this topic is still in its infancy. To date, a few studies have examined the integration of UGC and SAR for ISA mapping, and thus, further studies are necessary to address this topic.

Based on the aforementioned analysis, this study aims to assess the feasibility and advantages of a synergetic use of UGC and SAR data for ISA classification. The rest of this article is organized as follows. Section II presents the proposed approach and its phases. Section III describes the experimental results of two cases. Section IV discusses the findings, and finally, Section V concludes the study and gives a few recommendations.

II. PROPOSED APPROACH

The presented methodology consists of the following three main steps:

1) producing training samples for ISA;
2) classifying SAR images using one-class classifiers (OCCs); and
3) validation of the ISA maps by accuracy assessment. Each step is introduced in one of the following sections.

A. *Automatic Generation of Training Samples for ISA*

The first step in the process after downloading UGC data is to preprocess raw UGC data which involve three main parts—clipping, geographic coordinate system projection, and rasterization (see Fig. 1). In this study, UGC was collected from multiple platforms, including social media data from Twitter and Weibo, whereas POIs were collected from Google Maps and VGI from OSM. The collected raw UGC datasets usually have a larger geographical coverage than the study area, for example, covering an entire country. Thus, the UGC must be clipped to the study area to reduce the data size, enhancing the efficiency of the rest of the process.

Another issue of raw UGC is that the geographic coordinate systems of UGC and remote sensing imagery are often different,

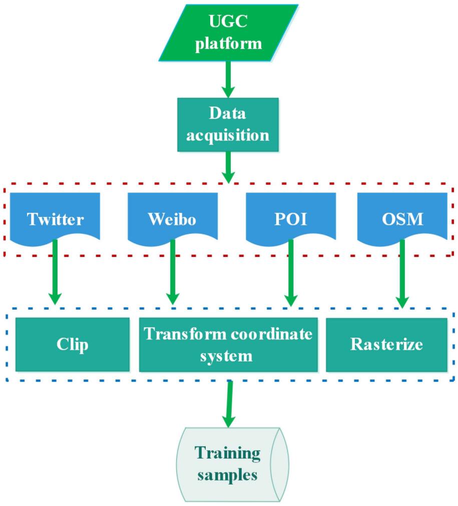

Fig. 1. Flowchart of preprocessing UGC data.

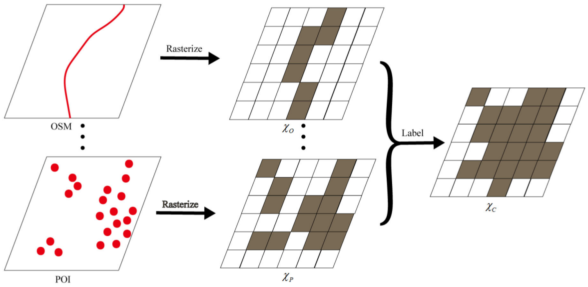

Fig. 2. Flowchart of automatic generation of training samples of ISA class from UGC.

for example, raw geo-location information for Weibo is recorded according to a specific geographic coordinate system (so-called GCJ-02). GCJ-02 is different from the SAR data with its WGS-84 geographic coordinate system. Previous studies show that the position offset/shift between GCJ-02 and WGS-84 ranges from 100 to 700 m [59]. Thus, the raw coordinates of UGC should be projected onto the satellite image coordinate system. After data clipping and coordinate system projection, the final step of the preprocessing is to rasterize the UGC (see Fig. 2). The grid size of the output raster is set to the spatial resolution of SAR data. In general, many UGC data may fall into a grid cell of the newly generated raster. For instance, users may send multiple tweets/microblog texts through different social media Apps at the same location, resulting in duplicated points in the UGC grid [46]. A thresholding procedure is applied to label training samples from duplicated points. If the amount of UGC in a grid is larger than the threshold, then this grid will be labeled as a training sample of the ISA class. However, the optimal threshold is challenging to set and can greatly vary across different study areas. Attribute values of UGC (e.g., text and picture) can provide complementary information to aid ISA training sample labeling. However, mining information from attribute values will complicate the task and increase computational complexity. To tackle these issues, this study presents a straightforward way to automatically produce training samples of ISA class from UGC. The pixels that contain UGC are labeled as training samples of the ISA class. As only geolocation information of UGC is involved, the presented strategy is very simple but effective.

According to the presented automatic training sample generation algorithm, four training sample sets are produced in this study as follows:

1) χ_T: the training sample set produced by considering only Twitter data;
2) χ_W: the training sample set produced by considering only Weibo data;
3) χ_O: the training sample set produced by considering only OSM data; and
4) χ_P: the training sample set produced by considering only POI data.

No UGC penetrated in the specific area and only SAR data are available in extreme circumstances. Hence, we can generate training samples χ_B using local indicators of spatial association (LISA) given that most ISA exhibits high backscattering values on SAR data [60]. Finally, a compound training set χ_C is generated by combining training samples from UGC and SAR data.

1) $\chi_C = \{\chi_T, \chi_W, \chi_O, \chi_P, \chi_B\}$: the combination set of $\chi_T, \chi_W, \chi_O, \chi_P$, and χ_B.

As only the class of ISA is to be derived from UGC and the class of pervious surface area is vacant during the training stage, OCC is utilized for classifying ISA from SAR images. This study selects a one-class support vector machine (OCSVM), and clustering-based OCSVM (C_OCSVM) to carry on ISA classification of SAR data. The rational to select different OCCs is to compare their robustness to training samples from different sources. Each classifier is introduced in detail as follows.

B. *One-Class Support Vector Machine*

Let $D = \{\boldsymbol{x}_i\}_{i=1}^{n}, \boldsymbol{x}_i \in {}^{N}$ denote the training dataset, and ϕ denotes a nonlinear mapping function

$$\phi : \mathbb{R}^N \rightarrow \chi \tag{1}$$

where N is the dimension of the feature vector and ϕ is the function that maps (via a kernel function) the training vectors from input space $\mathbb{R}^N$ into a high-dimensional feature space χ. In the high-dimensional feature space χ, a hyperplane can be established as

$$w\phi(\boldsymbol{x}) - \rho = 0 \tag{2}$$

where w is the vector normal to the hyperplane and ρ defines the distance of the hyperplane from the origin. The idea of the OCSVM is to iteratively find the maximal margin hyperplane that best discriminates the training data from the origin [61]. The slack variables ξ_i are introduced to improve the robustness of the algorithm, and the formulation of the OCSVM optimization problem is further expressed as

$$\min_{w,b,\xi_i} \left(\frac{1}{2} \| w\|^2 + \frac{1}{vn} \sum_{i=1}^{n} \xi_i - \rho \right)$$
$$\text{s.t. } (w \bullet \phi(\boldsymbol{x}_i)) \geqslant \rho - \xi_i \text{ and } \xi_i \geqslant 0 \; \forall i \tag{3}$$

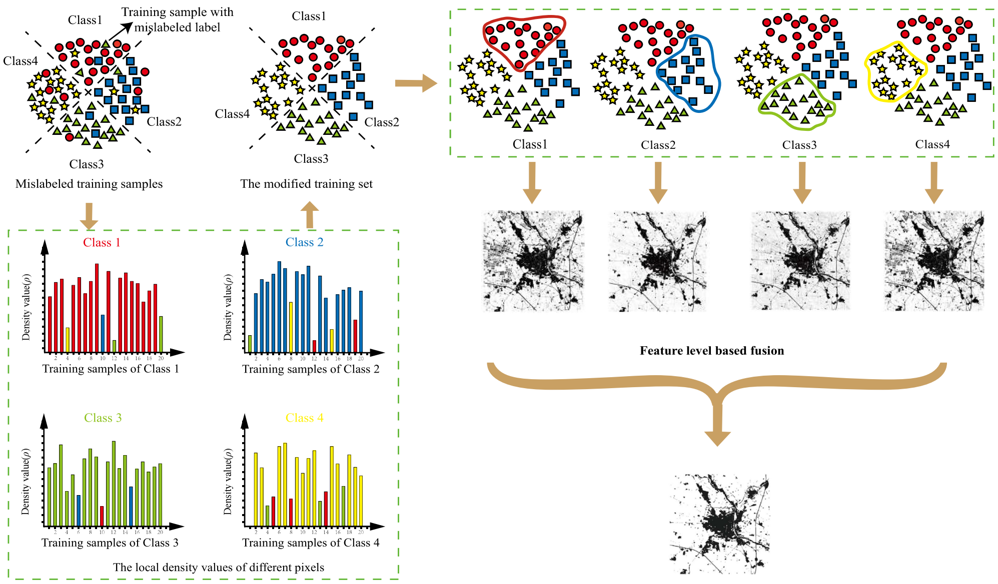

Fig. 3. Overall architecture of the proposed C_OCSVM.

where ν is the percentage of samples considered as outliers. The Lagrange function is introduced to solve the quadratic programming problem of (3) as follows:

$$L_P = \frac{1}{2}\|w\|^2 + \frac{1}{vn}\sum_{i=1}^{n}\xi_i - \rho - \sum_{i=1}^{n}\xi_i\beta_i - \sum_{i=1}^{n}\left(\left(w\phi\left(\boldsymbol{x}_i\right)\right) - \rho + \xi_i\right)\alpha_i \quad (4)$$

where α_i are the Lagrange multipliers. The dual form of (4) is as follows:

$$\min_{a_i} L_D = \frac{1}{2}\sum_{i=1}^{n}\sum_{j=1}^{n} a_i a_j K\left(\boldsymbol{x_i}, \boldsymbol{x_j}\right)$$

$$\text{s.t. } 0 \leqslant a_i \leqslant \frac{1}{vm} \text{ and } \sum_{i=1}^{n} a_i = 1. \quad (5)$$

After solving the optimization problem, the classification rule is defined

$$f\left(\boldsymbol{x}\right) = \operatorname{sgn}\left\{\sum_{i=1}^{n}\alpha_i K\left(\boldsymbol{x}, \boldsymbol{x}_i - \rho\right)\right\} \quad (6)$$

and a sample $\boldsymbol{x}$ is labeled as belonging to the ISA class if $f(\boldsymbol{x}) > 0$; otherwise, the sample will be labeled as the previous class.

Radial basis function (RBF) and linear kernel function are commonly used kernel functions. The RBF is also known as the Gaussian kernel and allows determining the radius of the hypersphere according to the parameter γ. The RBF is expressed by

$$K\left(\boldsymbol{x}, \boldsymbol{x}_i\right) = \exp\left(-\gamma d\left(\boldsymbol{x}, \boldsymbol{x}_i\right)\right) \quad (7)$$

where $d(\boldsymbol{x}, \boldsymbol{x}_i)$ is the distance between the sample $\boldsymbol{x}$ and the training sample $\boldsymbol{x}_i$, whereas γ is the kernel parameter.

Instead, the linear kernel function is the simplest kernel function that is given by the inner product

$$K\left(\boldsymbol{x}, \boldsymbol{x}_i\right) = \boldsymbol{x} \cdot \boldsymbol{x}_i. \quad (8)$$

The optimal parameters for OCSVM are obtained through fivefold cross-validation.

C. *Clustering-Based OCSVM*

Previous studies show that finding the best fitting hyperplane is challenging for OCSVM partly due to high-dimensional feature space, the lack of false-positive training sample, and/or the limitation of using a single classifier. Particularly, achieving the best balance between the model complexity and the classification accuracy is difficult for training samples with a large sample size [61]. Training OCSVM using a reduced feature set and/or a reduced sample size has proved to reduce the model complexity and help avoid overfitting the training samples. Hence, training OCSVM generally significantly decreases the classification accuracy [62]. Recent studies suggest that the combination of many OCC models can mitigate the aforementioned negative effects to a certain extent, thereby inspiring this study to present a C_OCSVM.

The proposed architecture of C_OCSVM consists of four main steps (see Fig. 3).

1) *Cluster training samples:* In this step, the entire training sample set is divided into N classes based on the landmark-based spectral clustering (LSC) [63]. LSC is selected due to its good performance and efficiency for large-scale clustering problems. The main idea of LSC is to find landmarks to establish a sparse representation of the original dataset. The final discrete clustering result is generated from the eigenvectors of the sparse representation matrix using *K-means*. Considering that the sample size of representative data (i.e., landmarks) is smaller than that of the original one, the computation cost of LSC is

significantly reduced with respect to any clustering applied to the original data set. Two parameters of LSC, that is, the number of landmarks (p) and the number of nearest landmarks (r), are required to be set by users. In this study, they are set to $p = 200$ and $r = 8$ given that the performance of LSC is robust to the parameter selection [64]. The number of clusters is set to $N = 4$ heuristically but, once again, any number larger than 4 works equally well.

2) *Compress label noise for a specific class:* Training samples of the ISA class directly derived from UGC inherently involve a certain amount of noise as UGC can be distributed in impervious (e.g., inside a building) and pervious areas (e.g., on the shores of a lake). This issue is exacerbated by a considerable number of UGC sets without any quality control, and classifiers must have the capability to deal with such a challenge. OCC tends to memorize several noisy labels and thus is prone to degrade its generalization performance [64]. To tackle this issue, a local outlier factor (LOF) is introduced to reduce the noise in the training samples. Specifically, after comparing the local density values of a sample to its neighbors, the sample that has a lower density than densities of their neighbors (i.e., LOF $\gg 1$) is taken as the outlier and subsequently removed. In this study, the number of neighbors is set to 20.
3) *Train an OCSVM model for each class:* In this step, each class extracted by the previous steps is considered independently obtained through a classification task, and thus, OCSVM is applied to the extraction of each of these classes individually. For each class, OCSVM is trained on the training samples of that class to find the optimal parameters as introduced in the previous section. After training OCSVM models on all sub-classes, numerous classification results from these N classifiers are produced.
4) *Combine multiple classification results:* After the classification step, N separate classification results are obtained. The final classification label is produced using the majority voting rule.

D. Accuracy Assessment

This study uses four measures to assess the performance of the presented method, including

$$OA = \frac{TN + TP}{TN + FN + TP + FP} \tag{9}$$

$$\text{precision} = \frac{TP}{TP + FP} \tag{10}$$

$$\text{recall} = \frac{TP}{FP + FN} \tag{11}$$

$$F_1 = 2 \cdot \frac{\text{precisionrecall}}{\text{precision+recall}} \tag{12}$$

where TP, TN, FP, and FN mean true positives, true negatives, false positives, and false negatives, respectively, and OA denotes the overall accuracy (OA). In this study, 200 test points are randomly selected for each class as ground truth by visual interpretation of high-resolution satellite imagery utilizing Google Earth to assess the classification accuracy.

TABLE I
List of Abbreviations Used in This Study

Abbreviation	Meaning
SAR	Synthetic-Aperture Radar
UGC	User-generated Content
ISA	Impervious Surface Area
VGI	Volunteered Geographic Information
POI	Point of Interest
OSM	OpenStreetMap
OCC	One-class Classifier
LISA	Local Indicators of Spatial Association
OCSVM	One-class Support Vector Machine
C_OCSVM	Clustering-based OCSVM
RBF	Radial Basis Function
LSC	Landmark-based Spectral Clustering
LOF	Local Outlier Factor
OA	Overall Accuracy
SBRG	Seed-based Region Growing
DEM	Digital Elevation Model

III. Experiments

A. Data Sources and Materials

The approaches presented in this study have been tested in two cities—namely, Beijing and Taipei, China (see Fig. 4). Beijing, the capital of China, is located in northern China and has the characteristics of a typical Chinese city, which experienced rapid development since the 1980s. This region has witnessed China's urbanization process and is a microcosm of China's rapid population and economic growth. The other study area, Taipei city, is located in the northern Taiwan island. Taipei is a typical tropical city where the SAR image shows great advantage compared with optical remote sensing images due to its all-weather capacity.

Sentinel-1 SAR images of the two study areas were considered for the use of this study. The SAR images of Beijing and Taipei were level 1b single look complex products with interferometric wide swath mode, acquired on August 25, 2019 and October 20, 2018, respectively. The radiometric correction together with a mean filter procedure was performed to preprocess the SAR images. Then, the preprocessed SAR images were geocoded by using UTM projection with WGS84 datum. The Sentinel Application Platform is the main tool that worked in Intel Core i5-7400 CPU at 3.00 GHz and 8-GB RAM.

UGC data sources were selected to enable assessment of the performance and stability of different OCCs applied to different social media platforms to extract ISA from SAR images. Table II shows that UGC was collected from four different platforms, including geo-locations of Tweets and Weibo posts, road, and building layers of OSM, and POIs from Google Maps. Figs. 5 and 6 illustrate the spatial distributions of UGC data and LISA points for the two study areas. The distributions of collected tweets/Weibo posts are significantly different in the two cities. In Beijing, Weibo has a higher penetration rate

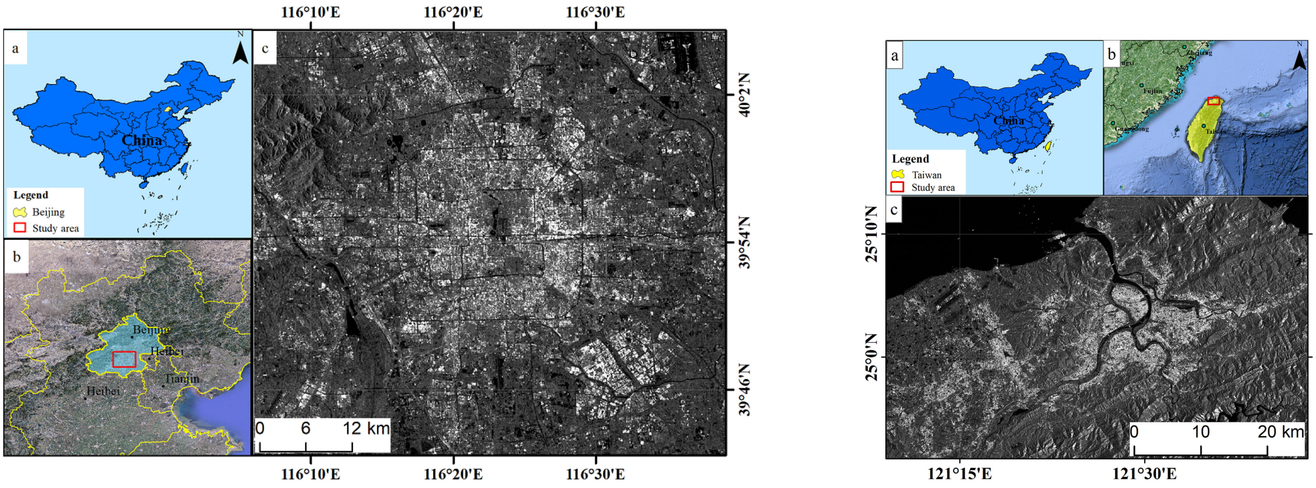

(a)

(b)

Fig. 4. Illustration of study areas. (a) Beijing. (b) Taipei.

TABLE II
UGCs and Satellite Images Used in This Study

Dataset description	Source	Year	Category
Geo-location of Tweets	Twitter API ®	2016	Social media
Geo-location of Weibo	Weibo API ®	2017	Social media
OSM roads and buildings	OpenStreetMap	2019	VGI
Points of interests	Google Maps®	2019	Public available
Mountain masks	Shuttle Radar Topography Mission digital elevation model	2019	Public available
SAR images	Sentinel	2019	Public available

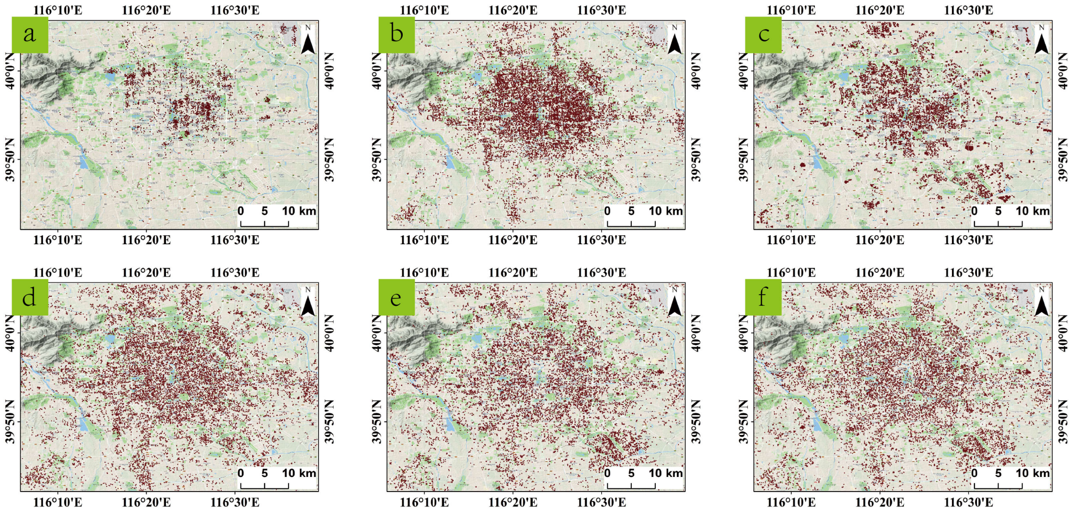

Fig. 5. UGC data were used in Beijing area. (a) χ_T, (b) χ_W, (c) χ_O, (d) χ_P, (e) χ_B, and (f) χ_C.

than Twitter, as the latter is censored in mainland China [see Fig. 5(a) and (b)]. By contrast, Twitter is more popular than Weibo in Taipei, making the number of tweets in the data denser than Weibo [see Fig. 6(a) and (b)]. Furthermore, social media data are concentrated in dense urban areas and scarce in rural/remote areas (see Figs. 5 and 6). Finally, compared with social media data, road, and building layers of OSM, POIs from Google Maps and LISA points have wider spatial coverage.

The mountainous area exhibits similar high backscatter to ISAs because of the steep slopes and complex terrains, leading to false positives that reduce the classifier performance. To tackle this issue, this study applies a slope image generated from Shuttle Radar Topography Mission (SRTM) digital elevation

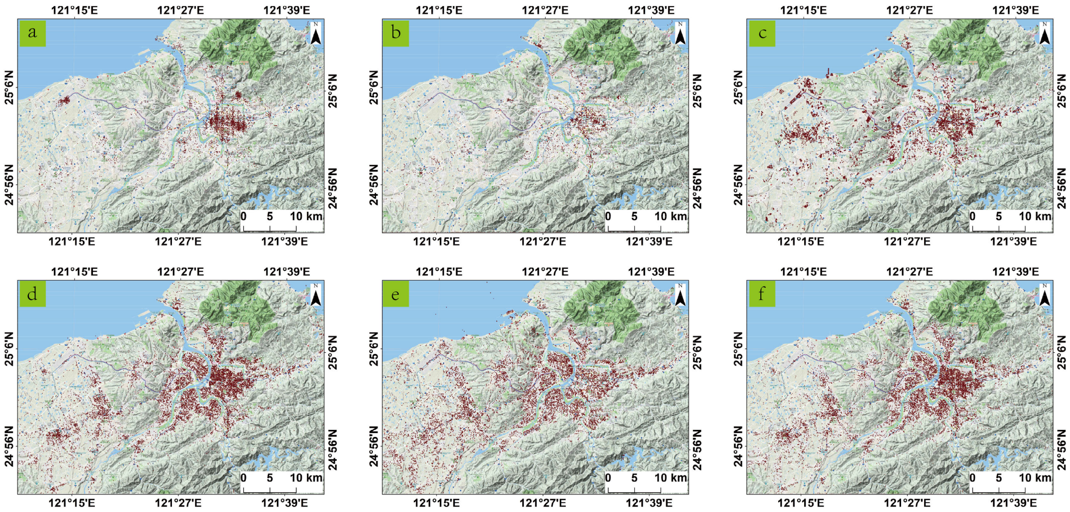

Fig. 6. UGC data were used in Taipei area. (a) χ_T, (b) χ_W, (c) χ_O, (d) χ_P, (e) χ_B, and (f) χ_C.

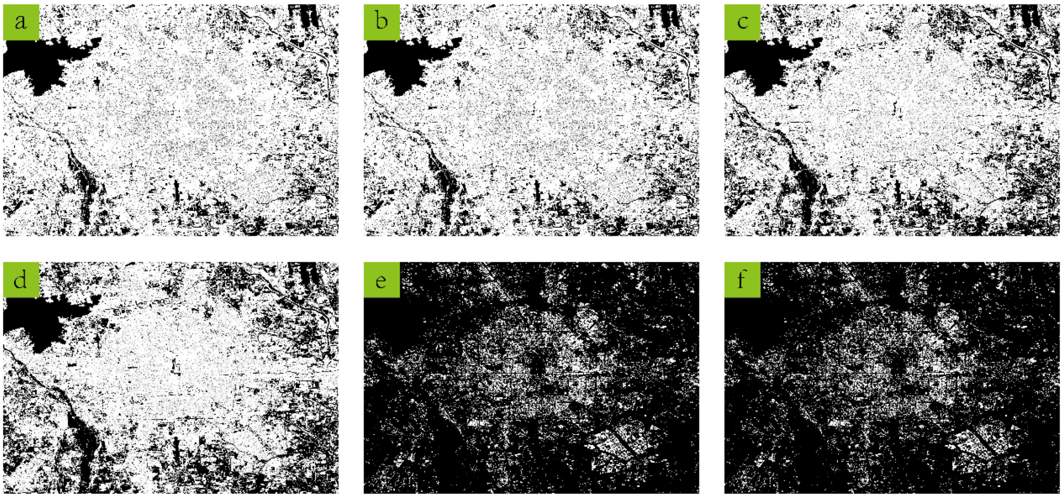

Fig. 7. ISA classification results using OCSVM with the Gaussian kernel based on (a) χ_T, (b) χ_W, (c) χ_O, (d) χ_P, (e) χ_B, and (f) χ_C, respectively, for the Beijing test site.

model (DEM) with a spatial resolution of 30 m to mask out pixels located in the mountainous area. Ban *et al.* [15] noted that a slope threshold of 15° is set, that is, an area with the slope greater than 15° is considered a mountainous area and masked out.

B. Results

Compared with OCSVM and C_OCSVM, a seed-based region growing (SBRG) [65] approach is used. SBRG is a simple image segmentation method and has been widely used to extract ISA from SAR images. Figs. 7–11 show the ISA classification results in Beijing by using OCSVM, C_OCSVM, and SBRG based on six training sample generation strategies (i.e., χ_T, χ_W, χ_O, χ_P, χ_B, and χ_C). Table III reports the corresponding accuracy evaluation results for the Beijing case. Figs. 12–16 and Table IV show the ISA classification results by using OCSVM, C_OCSVM, and SBRG and the accuracy evaluation results, respectively, for the Taipei case.

For OCSVM and C_OCSVM, the use of the linear kernel leads to better and highly robust results than the use of the Gaussian kernel. The classification results of OCSVM and C_OCSVM with Gaussian kernel vary greatly with different training sample generation strategies and contain large over- and under-estimations of the ISA (Figs. 7, 9, 12, and 14). By contrast, OCSVM and C_OCSVM with the linear kernel are capable to generate highly consistent ISA classification results by using different training sample generation strategies (Figs. 8, 10, 13, and 15). The OA of the OCSVM and C_OCSVM classification results with Gaussian kernel, specifically that of C_OCSVM, is also significantly lower than that of the OA with the linear kernel (Tables III and IV). The rest of this section will focus on the results with a linear kernel when referring to OCSVM and C_OCSVM.

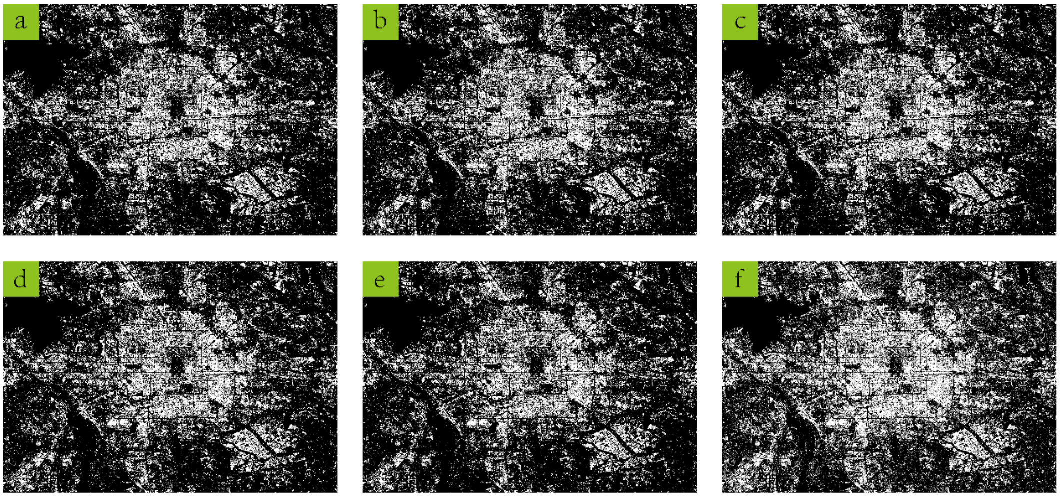

Fig. 8. ISA classification results using OCSVM with the linear kernel based on (a) χ_T, (b) χ_W, (c) χ_O, (d) χ_P, (e) χ_B, and (f) χ_C, respectively, for the Beijing test site.

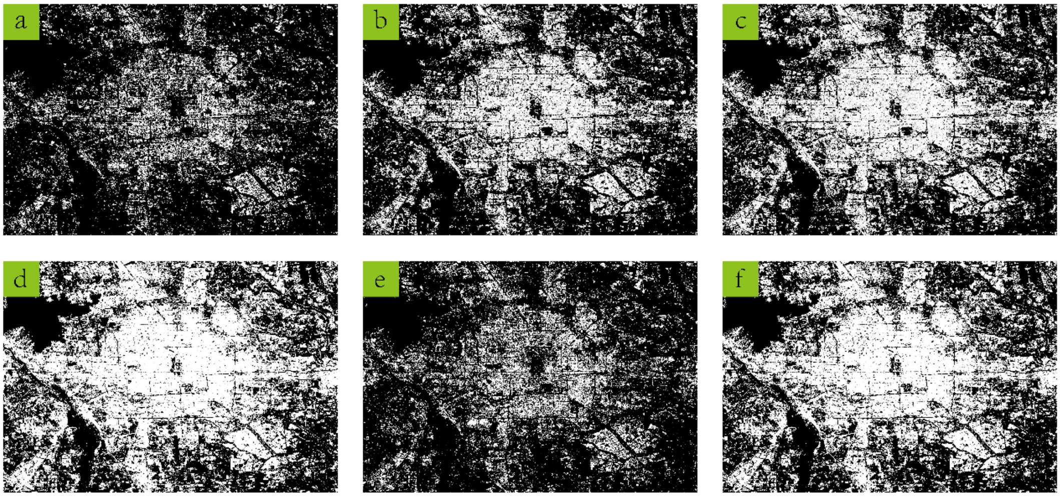

Fig. 9. ISA classification results using C_OCSVM with the Gaussian kernel based on (a) χ_T, (b) χ_W, (c) χ_O, (d) χ_P, (e) χ_B, and (f) χ_C, respectively, for the Beijing test site.

Tables III and IV suggest that the combination of all available UGC and χ_B from SAR images does not necessarily obtain high accuracy. C_OCSVM based on one UGC is sufficient to produce satisfactory ISA results. Particularly, POI and OSM are more beneficial for C_OCSVM than Twitter and Weibo as they generally produce more satisfactory result. This is because that the first two UGC sources are intentionally to associate with geo-location information, thereby concerning the data quality of geo-location, which in turn reduces the error of training samples derived from POI and OSM.

Compared with OCSVM and C_OCSVM, SBRG classification results are less noisy, as this approach involves a mathematical morphological filtering step. The selection of the training sample generation strategy still has an influence on the classification performance. On the other hand, C_OCSVM with the auxiliary UGC can achieve comparable or higher accuracy compared to that only using χ_B from SAR images. The combination of UGC and SAR images is more efficient than only using χ_B from SAR images as the extraction of χ_B from SAR images is particularly computational costly, making it not suitable for regional/global ISA mapping. However, χ_B can be supplementary data source when UGC is vacant or sparse in some areas (e.g., remote rural areas). We will discuss this issue in the following section.

C. Classification Accuracy and Robustness

Compared with the two alternative methods, the newly proposed C_OCSVM shows a clear advantage in accurate classifications with different training sample sets. This method has significantly higher robustness to the strategies and data used to generate the training samples, although it does not provide the most accurate result when the combined training sample set χ_C is used. Among the classification results with the other five

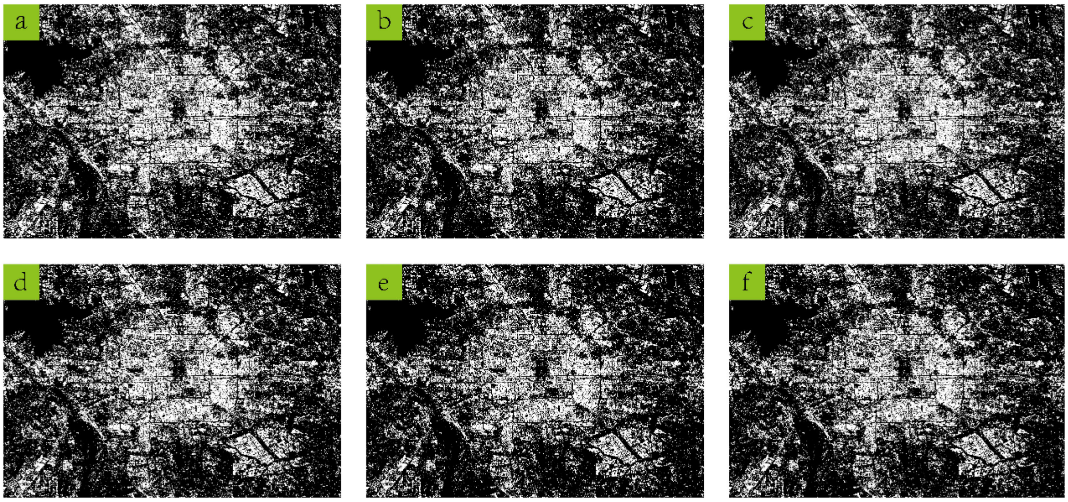

Fig. 10. ISA classification results using C_OCSVM with the linear kernel based on (a) χ_T, (b) χ_W, (c) χ_O, (d) χ_P, (e) χ_B, and (f) χ_C, respectively, for the Beijing test site.

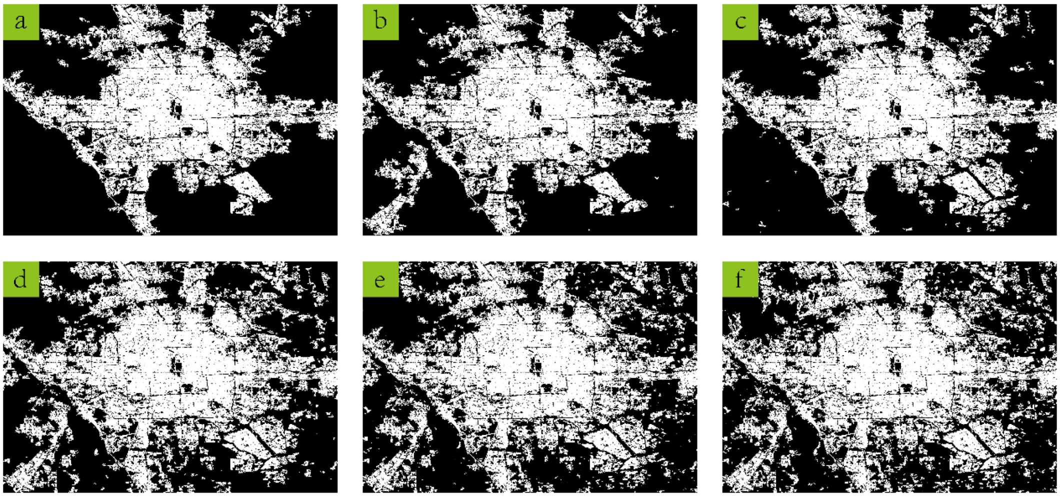

Fig. 11. ISA classification results using SBRG based on (a) χ_T, (b) χ_W, (c) χ_O, (d) χ_P, (e) χ_B, and (f) χ_C, respectively, for the Beijing test site.

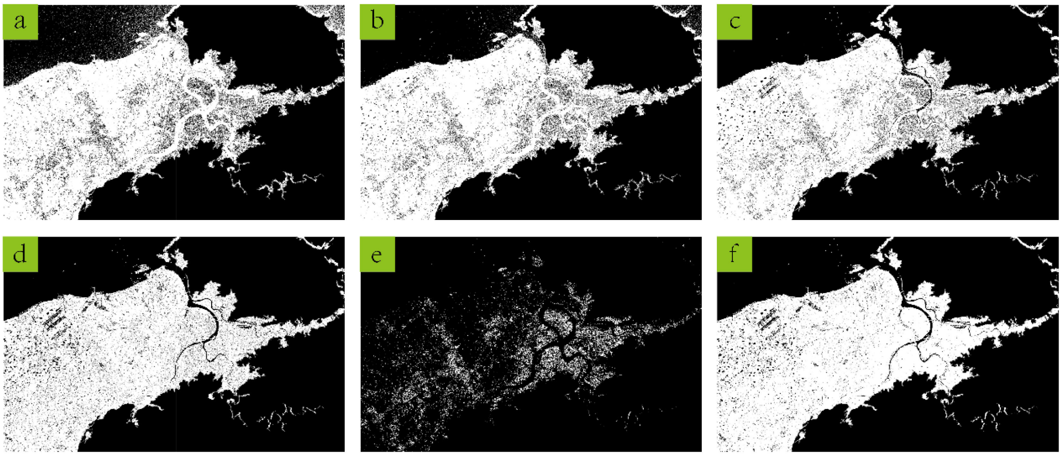

Fig. 12. ISA classification results using OCSVM with the Gaussian kernel based on (a) χ_T, (b) χ_W, (c) χ_O, (d) χ_P, (e) χ_B, and (f) χ_C, respectively, for the Taipei test site.

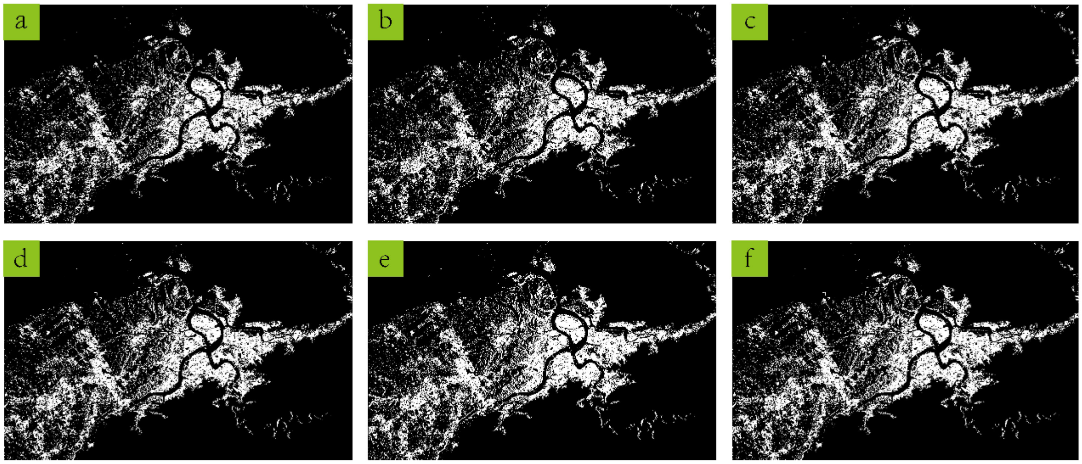

Fig. 13. ISA classification results using OCSVM with the linear kernel based on (a) χ_T, (b) χ_W, (c) χ_O, (d) χ_P, (e) χ_B, and (f) χ_C, respectively, for the Taipei test site.

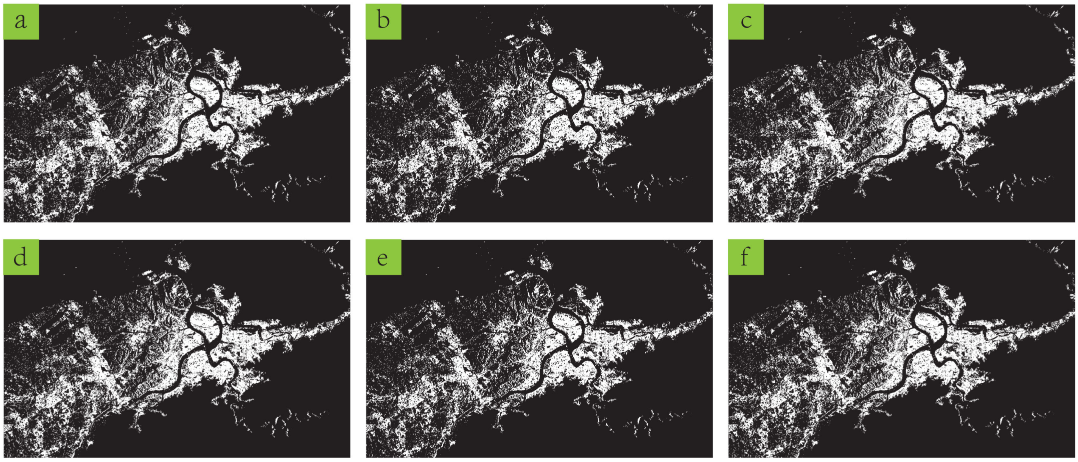

Fig. 14. ISA classification results using C_OCSVM with the Gaussian kernel based on (a) χ_T, (b) χ_W, (c) χ_O, (d) χ_P, (e) χ_B, and (f) χ_C, respectively, for the Taipei test site.

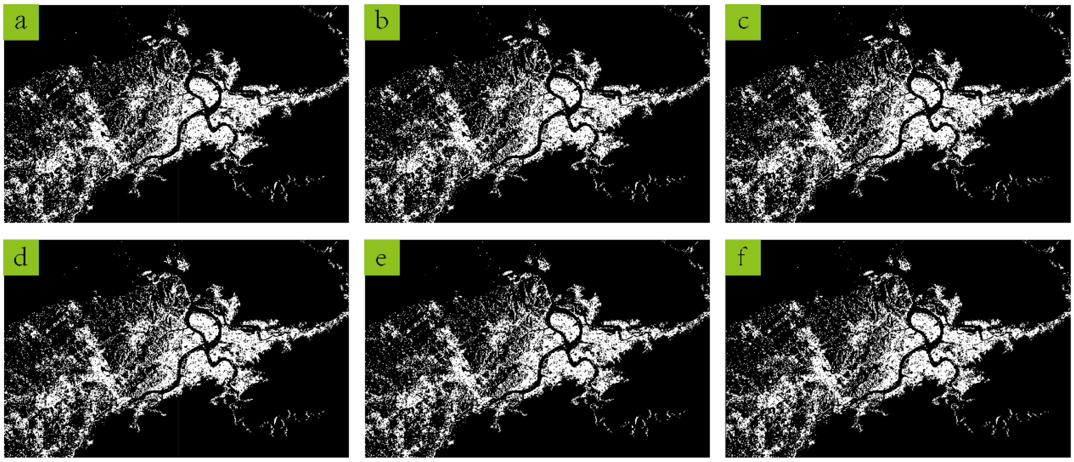

Fig. 15. ISA classification results using C_OCSVM with the linear kernel based on (a) χ_T, (b) χ_W, (c) χ_O, (d) χ_P, (e) χ_B, and (f) χ_C, respectively, for the Taipei test site.

TABLE III
Classification Performance of OCSVM, C_OCSVM, and SBRG Based on χ_T, χ_W, χ_O, χ_P, χ_B, and χ_C for Beijing Case

Method	Metric	χ_T	χ_W	χ_O	χ_P	χ_B	χ_C
OCSVM (Gaussian kernel)	OA	0.5866	0.5943	0.6615	0.6848	0.6253	0.6124
	F_1	0.6813	0.6841	0.7299	0.7415	0.4358	0.4048
	Precise	0.5552	0.5611	0.6082	0.6295	0.8889	0.8793
	Recall	0.8814	0.8763	0.9124	0.9021	0.2887	0.2629
OCSVM (linear kernel)	OA	0.6822	0.7313	0.7597	0.7335	0.6951	0.7700
	F_1	0.5650	0.7030	0.7580	0.7640	0.5990	0.7855
	Precise	0.8990	0.7880	0.7640	0.6850	0.8800	0.7376
	Recall	0.4124	0.6340	0.7526	0.8632	0.4536	0.8402
C_OCSVM (Gaussian kernel)	OA	0.7235	0.7313	0.7313	0.7313	0.7132	0.7313
	F_1	0.6603	0.6730	0.6730	0.6730	0.6408	0.7011
	Precise	0.8595	0.8629	0.8629	0.8629	0.8609	0.7922
	Recall	0.5361	0.5515	0.5515	0.5515	0.5103	0.6289
C_OCSVM (linear kernel)	OA	0.7416	0.7416	0.7416	0.7416	0.7313	0.7313
	F_1	0.6894	0.6894	0.6894	0.6970	0.6730	0.6730
	Precise	0.8672	0.8672	0.8672	0.8456	0.8629	0.8629
	Recall	0.5722	0.5722	0.5722	0.5928	0.5515	0.5515
SBRG	OA	0.6486	0.6589	0.6899	0.7571	0.7339	0.7649
	F_1	0.5776	0.6118	0.6512	0.7552	0.7268	0.7684
	Precise	0.7266	0.7123	0.7467	0.7632	0.7486	0.7588
	Recall	0.4794	0.5361	0.5773	0.7474	0.7062	0.7784

TABLE IV
Classification Performance of OCSVM, C_OCSVM, and SBRG Based on χ_T, χ_W, χ_O, χ_P, χ_B, and χ_C for Taipei Case

Method	Metric	χ_T	χ_W	χ_O	χ_P	χ_B	χ_C
OCSVM (Gaussian kernel)	OA	0.3898	0.4407	0.4520	0.5537	0.6949	0.5932
	F_1	0.5221	0.5714	0.5837	0.6638	0.5574	0.7073
	Precise	0.4245	0.4583	0.4658	0.5270	0.9714	0.5472
	Recall	0.6782	0.7586	0.7816	0.8966	0.3908	1.0000
OCSVM (linear kernel)	OA	0.8588	0.8588	0.8701	0.8701	0.8870	0.8701
	F_1	0.8428	0.8428	0.8589	0.8589	0.8824	0.8589
	Precise	0.9306	0.9306	0.9211	0.9211	0.9036	0.9211
	Recall	0.7701	0.7701	0.8046	0.8046	0.8621	0.8046
C_OCSVM (Gaussian kernel)	OA	0.8701	0.8588	0.8814	0.8870	0.8531	0.8701
	F_1	0.8589	0.8428	0.8743	0.8795	0.8375	0.8589
	Precise	0.9211	0.9306	0.9125	0.9241	0.9178	0.9211
	Recall	0.8046	0.7701	0.8391	0.8391	0.7701	0.8046
C_OCSVM (linear kernel)	OA	0.8814	0.8814	0.8870	0.8870	0.8870	0.8870
	F_1	0.8772	0.8772	0.8837	0.8837	0.8824	0.8837
	Precise	0.8929	0.8929	0.8941	0.8941	0.9036	0.8941
	Recall	0.8621	0.8621	0.8736	0.8736	0.8621	0.8736
SBRG	OA	0.8588	0.8136	0.8531	0.8588	0.8927	0.8927
	F_1	0.8503	0.7843	0.8452	0.8503	0.8876	0.8927
	Precise	0.8875	0.9091	0.8765	0.8875	0.9146	0.8778
	Recall	0.8161	0.6897	0.8161	0.8161	0.8621	0.9080

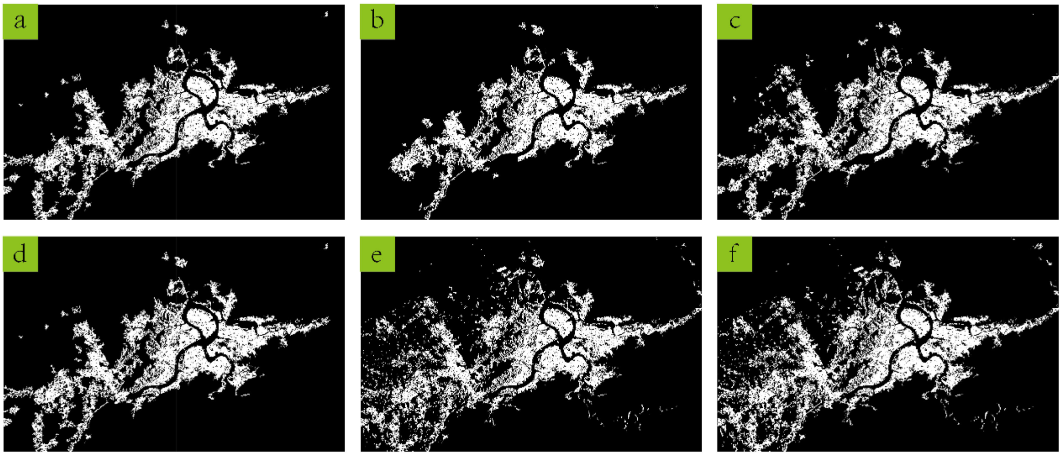

Fig. 16. ISA classification results using SBRG based on (a) χ_T, (b) χ_W, (c) χ_O, (d) χ_P, (e) χ_B, and (f) χ_C, respectively, for the Taipei test site.

training sample set χ_C, for the Beijing test site, C_OCSVM (linear kernel) achieved higher OA values than OCSVM (linear kernel) and SBRG for four and three training sample sets (see Table III). For the Taipei test site, C_OCSVM (linear kernel) achieved larger OA values than OCSVM (linear kernel) and SBRG for four training sample sets (see Table IV). In the Beijing test site, the difference between the results with the highest and lowest OA values produced by using the six training sample generation strategies is only 1.03% for C_OCSVM (linear kernel), 8.78% for OCSVM (linear kernel), and 11.63% for SBRG. In the Taipei test site, the difference in OA values is 0.56% for C_OCSVM (linear kernel), 2.82% for OCSVM (linear kernel), and 7.91% for SBRG. That is, the fluctuation in OA for C_OCSVM due to different training sample generation strategies is approximately one-tenth to one-fifth of the one for OCSVM and SBRG.

In the real production of large-scale ISA maps, collecting various types of UGC and thereby conducting the classification on a combined χ_C as comprehensive as in this experiment are rather laborious, and using one or two individual training sample sets will be highly feasible. In this case, C_OCSVM has the highest chance to produce the most accurate classification results and bears the lowest risk, among the three experimented methods, in generating unexpectedly low accuracy due to the sensitivity to the training sample generation strategies.

C_OCSVM has significantly higher robustness to training samples than the two alternative methods likely because of its use of N classifiers from N clusters of training samples. The final classification results from the majority voting of the N classification results can greatly reduce the misclassification due to individual elements in the training samples that are mislabeled or inappropriately assigned to a specific class. Moreover, each cluster of training samples contains reduced information as compared with the entire training sample set. On some occasions, where the entire training sample set was able to result in highly accurate results, the C_OCSVM and SBRG could lead to a better result than OCSVM, as shown in Tables III and IV. Among various training sample generation strategies, the overall classification accuracy of C_OCSVM is generally better than the one of OCSVM and comparable with the one of SBRG.

For all three methods, the classification results in the Taipei test site were more accurate than those in the Beijing test site. A possible reason is that the urban structure parameter, such as building height, has considerable influence in urban backscattering characteristics. Compared with the Beijing case, Taipei is a small city, and the building height is relatively uniform, leading to more homogeneous double-bounce scattering that benefits ISA mapping.

D. Effect of the Use of UGC and Data Integration on Classification Accuracy

The sole use of training samples generated from UGC did not improve the classification accuracy, compared with the training samples from the SAR images (i.e., χ_B). In the Beijing test site, the OCSVM (linear kernel) classification results with UGC-based training samples were more accurate than those with χ_B (see Table III). However, for the OCSVM (linear kernel) in the Taipei test site and SBRG in both test sites, the results using χ_B were highly accurate (see Tables III and IV). For C_OCSVM, UGC-based training samples and χ_B resulted in very similar classification accuracy values, as mentioned in Section 3.2.1. Among the UGC-based training sample sets, samples from OSM buildings and roads (χ_O) and Google Maps POIs (χ_P) generally resulted in higher classification accuracy than the samples from geo-located social media posts (χ_T, χ_W). The social media geo-localization is likely more inaccurate than VGI buildings and roads and POIs, at least in terms of its usefulness for representing ISA. For example, people tend not to geotag their home locations or deserted factory areas which indeed belong to ISA, and may geotag natural scenic spots in previous areas.

The combination of training samples from different data sources or platforms, that is, χ_C, shows appreciable enhancements to the classification accuracy only for OCSVM and SBRG. In the Beijing test site, OCSVM (linear kernel) and SBRG generated the best classification performance using χ_C, among all training sample sets. However, for OCSVM (linear kernel) and SBRG in the Taipei test site, the classification accuracy with individual UGC platforms already exceeded 0.8, and C_OCSVM is highly robust to the training sample generation strategies. Nevertheless, the classification results with χ_C were not more accurate than the best results among those with the other five training sample sets.

E. Computational Performance

Table V shows the computational loads of C_OCSVM and SBRG for both study areas under different experimental settings. As accurately described in Section IV-B, the classification accuracy of C_OCSVM is almost constant with the increase of training sample size from 2000 to 14 000. Thus, the training sample size of 2000 for C_OCSVM, which has the least computational cost, is recommended. In this case, the time consumption of SBRG is ten to hundreds of times higher than that of C_OCSVM (see Table V). Specifically, the time cost of SBRG increases sharply for large training samples. The computational time for SBRG using the combined training sample set χ_C which yields the highest classification accuracy was approximately 400 times than that for C_OCSVM in the Beijing test site, and over 50 times than that for C_OCSVM in the Taipei test site. By contrast, C_OCSVM not only significantly speeds up ISA classification of SAR data, but is also highly scalable. The advantage of C_OCSVM in computational efficiency, together with its comparable accuracy with SBRG, suggests the great potential of C_OCSVM for large-scale regional, national, or global ISA mapping.

IV. DISCUSSIONS

A. Investigation of Training Sample Size Effect on C_OCSVM

We trained C_OCSVM on different training sample sizes, varying from 2000 to 14 000 with an interval of 3000, to explore the influence of the training sample size on the performance of C_OCSVM. A linear kernel was selected as the kernel function of C_OCSVM, and Table VI shows the results.

TABLE V
COMPARISON OF COMPUTATION EFFICIENCY OF C_OCSVM AND SBRG

Study area	Size	C_OCSVM (s)						SBRG (s)					
		χ_T[1]	χ_W	χ_O	χ_P	χ_B	χ_C	χ_T	χ_W	χ_O	χ_P	χ_B	χ_C
Beijing	2,000	72	70	84	72	75	114	2,340	3,060	1,800	3,420	21,300	44,760
	5,000	\	110	116	116	118	161						
	8,000	\	144	154	152	161	203						
	11,000	\	180	198	194	201	246						
	14,000	\	223	229	239	244	296						
Taipei	2,000	54	57	57	59	59	57	1,560	1,560	1,560	2,040	3,360	3,180
	5,000	\	\	88	84	87	96						
	8,000	\	\	164	115	116	115						
	11,000	\	\	192	244	243	250						
	14,000	\	\	241	290	280	285						

[1] The size of χ_T in Beijing and Taipei is 3000 and 3400, respectively. Thus, the training sample size larger than 5000 is not tested. For the same reason, the training sample size of χ_W in Taipei larger than 5000 is not tested.

TABLE VI
TEST OF THE TRAINING SAMPLE SIZE OF C_OCSVM ON DIFFERENT TRAINING SAMPLE GENERATION STRATEGIES

Sample set	Metric	Beijing					Taipei				
		2,000	5,000	8,000	11,000	14,000	2,000	5,000	8,000	11,000	14,000
χ_T[1]	OA	0.7364	\	\	\	\	0.8814	\	\	\	\
	F_1	0.7052	\	\	\	\	0.8772	\	\	\	\
	Precise	0.8026	\	\	\	\	0.8929	\	\	\	\
	Recall	0.6289	\	\	\	\	0.8621	\	\	\	\
χ_W	OA	0.7494	0.7313	0.7416	0.7313	0.7313	0.8814	\	\	\	\
	F_1	0.7069	0.6730	0.6894	0.6730	0.6730	0.8743	\	\	\	\
	Precise	0.8540	0.8629	0.8672	0.8629	0.8629	0.9125	\	\	\	\
	Recall	0.6031	0.5515	0.5722	0.5515	0.5515	0.8391	\	\	\	\
χ_O	OA	0.7364	0.7313	0.7313	0.7313	0.7416	0.8814	0.8870	0.8814	0.8870	0.8814
	F_1	0.7000	0.6730	0.6730	0.6730	0.6951	0.8743	0.8810	0.8743	0.8810	0.8743
	Precise	0.8151	0.8629	0.8629	0.8629	0.8507	0.9125	0.9136	0.9125	0.9136	0.9125
	Recall	0.6134	0.5515	0.5515	0.5515	0.5876	0.8391	0.8506	0.8391	0.8506	0.8391
χ_P	OA	0.7339	0.7416	0.7313	0.7313	0.7235	0.8870	0.8870	0.887	0.8814	0.8870
	F_1	0.6979	0.7110	0.6730	0.6730	0.6748	0.8810	0.8810	0.8810	0.8743	0.881
	Precise	0.8095	0.8092	0.8629	0.8629	0.8222	0.9136	0.9136	0.9136	0.9125	0.9136
	Recall	0.6134	0.6340	0.5515	0.5515	0.5722	0.8506	0.8506	0.8506	0.8391	0.8506
χ_B	OA	0.7416	0.7416	0.7313	0.7235	0.7313	0.8870	0.8870	0.887	0.8814	0.887
	F_1	0.6894	0.6894	0.6730	0.6687	0.6730	0.8795	0.8795	0.8795	0.8772	0.8795
	Precise	0.8672	0.8672	0.8629	0.8372	0.8629	0.9241	0.9241	0.9241	0.8929	0.9241
	Recall	0.5722	0.5722	0.5515	0.5567	0.5515	0.8391	0.8391	0.8391	0.8621	0.8391
χ_C	OA	0.7313	0.7313	0.7339	0.7313	0.8870	0.8870	0.8814	0.8870	0.8814	0.8814
	F_1	0.6790	0.6730	0.6771	0.6730	0.8810	0.8810	0.8757	0.8810	0.8743	0.8743
	Precise	0.8462	0.8629	0.8640	0.8629	0.9136	0.9136	0.9024	0.9136	0.9125	0.9125
	Recall	0.5670	0.5515	0.5567	0.5515	0.8506	0.8506	0.8506	0.8506	0.8391	0.8391

[1] The size of χ_T in Beijing and Taipei is 3000 and 3400, respectively. Thus, the training sample size larger than 5000 is not tested. For the same reason, the training sample size of χ_W in Taipei larger than 5000 is not tested.

Evidently, C_OCSVM is capable to yield consistent and stable results while the training sample size increased. For Beijing and Taipei test sites, the change of OA and F_1 values along the set of different sample sizes is insignificant: no clear trend or performance change is observed when the training sample size is altered. The reason is that most of the UGC is concentrated on impervious areas, and the percentage of UGC in pervious areas is very low. Thus, most of the training samples derived from UGC are correct and secure the success of the proposed method.

The insensitivity to the training sample size of C_OCSVM is expected to be particularly advantageous in terms of mitigating data gaps of UGC in some countries/regions (e.g., undeveloped countries or remote areas) and alleviating the workload necessary to collect various UGC data sets from different platforms. Particularly, in extreme cases, where no UGC data are available, we can still solely rely on SAR data, at the cost of low computational efficiency, to automatically generate training samples to implement the proposed method. Therefore, C_OCSVM can be applied to process SAR data even when no UGC data are available. This case in turn validates the practical value and feasibility of the proposed method in ISA mapping at the global or regional scale.

B. Test About the Influence of Data Quality of UGC on C_OCSVM

The geolocation quality cannot be guaranteed because crowdsourcing UGC is not collected for scientific research. Points from UGC were initially jittered by adding random noise (e.g., bias

TABLE VII
INFLUENCE OF DATA QUALITY OF UGC ON THE PERFORMANCE OF C_OCSVM

Study area	Bias (m)	0	10	20	30	40	50	60	70	80	90	100
Beijing	OA	0.7416	0.7339	0.7364	0.7339	0.7339	0.7339	0.7339	0.7364	0.7339	0.7339	0.7339
	F_1	0.7093	0.7066	0.7052	0.6979	0.7066	0.7066	0.7066	0.7052	0.7066	0.7066	0.7066
	Precise	0.8133	0.7898	0.8026	0.8095	0.7898	0.7898	0.7898	0.8026	0.7898	0.7898	0.7898
	Recall	0.6289	0.6392	0.6289	0.6134	0.6392	0.6392	0.6392	0.6289	0.6392	0.6392	0.6392
Taipei	OA	0.8870	0.8870	0.8814	0.8814	0.8814	0.8870	0.8870	0.8814	0.8814	0.8814	0.8814
	F_1	0.8810	0.8810	0.8757	0.8743	0.8743	0.8810	0.8810	0.8743	0.8743	0.8743	0.8743
	Precise	0.9136	0.9136	0.9024	0.9125	0.9125	0.9136	0.9136	0.9125	0.9125	0.9125	0.9125
	Recall	0.8506	0.8506	0.8506	0.8391	0.8391	0.8506	0.8506	0.8391	0.8391	0.8391	0.8391

changes from 10 to 100 m) to their geographical coordinates, followed by randomly selecting 2000 samples from the jittered training sample set to test the influence of UGC data quality on the performance of C_OCSVM. In this test, C_OCSVM with linear kernel was trained on a jittered sample set of χ_P. Table VII shows the evaluation results. For the Beijing test site, OA values range from 73.39% to 74.16% and F_1 values from 69.79% to 70.93%. For the Taipei test site, OA values vary from 88.14% to 88.70% and F_1 values from 87.43% to 88.10%. These results suggest that the influence of the UGC data quality on the performance of C_OCSVM is marginal.

C. Data Availability of UGC

A single data source of UGC in a specific area may suffer from the limited amount of data and uneven spatial distribution of training samples derived from UGC, thereby potentially decreasing the ISA mapping accuracy. The drawback of using a single UGC data source is that the risk of unstable ISA mapping results may be increased. Moreover, access to geo-referenced social media data (e.g., Facebook, Twitter, and WeChat) in large areas or via bulk download may not be publicly possible. Furthermore, access to such data usually requires an agreement with companies providing social media service, which is getting rather unlikely with regard to data leaks and user privacy protection issues. For instance, Weibo was freely streamed several years ago, but downloading a large number of Weibo data is now forbidden. Luckily, OSM and/or POI data should be stable and reliable open data sources.

V. CONCLUSION

ISA classification from satellite images is critical for a wide range of urban applications in developing countries where nature land is considerably changing to an impervious surface. To this end, this study integrates UGC and SAR satellite images to produce ISA maps. Specifically, UGC is utilized to automatically generate training samples of the ISA class to train a pool of OCCs. This study also designed a so-called C_OCSVM to alleviate the influence of UGC sources and training sample size. Experimental results have proven the usefulness of UGC in producing reliable training samples to improve the performance of traditional SAR processing algorithms (e.g., SBRG). C_OCSVM also greatly improves the computational efficiency and offers important complementary information to improve ISA classification accuracy, making it a viable solution to estimate and map imperviousness at the global/regional scale.

In the future, although the proposed method was applied to SAR images, this method is also partially suitable to process optical satellite images with a similar processing chain. The combined use of SAR, optical images, and user-generated data is an interesting research direction.

Moreover, the proposed method only extracts ISA maps from a single SAR image. However, the integration of multitemporal ascending and descending pass SAR intensity and coherence information is expected to further improve the ISA classification accuracy. Further attention should be paid in future studies to consider multitemporal SAR images.

ACKNOWLEDGMENT

The authors would like to thank Prof. Q. Du from Mississippi State University for her kind discussions on this article. The authors would also like to thank two anonymous reviewers for their constructive comments that greatly improve this article.

REFERENCES

[1] L.-I. Mccall *et al.*, "Home chemical and microbial transitions across urbanization," *Nat. Microbiol.*, vol. 5, no. 1, pp. 108–115, 2020.

[2] W. Zhang, G. Villarini, G. A. Vecchi, and J. A. Smith, "Urbanization exacerbated the rainfall and flooding caused by hurricane Harvey in Houston," *Nature*, vol. 563, no. 7731, pp. 384–388, 2018.

[3] L. K. McDonough *et al.*, "Changes in global groundwater organic carbon driven by climate change and urbanization," *Nat. Commun.*, vol. 11, no. 1, pp. 1–10, 2020.

[4] P. Prastacos and N. Chrysoulakis, "Urban Atlas, land use modelling and spatial metric techniques," in *Proc. Eur. Regional Sci. Assoc. Conf.*, Sep. 2011, Paper ersa11p1406. [Online]. Available: https://ideas.repec.org/p/wiw/wiwrsa/ersa11p1406.html

[5] J. Chen, X. Cao, S. Peng, and H. Ren, "Analysis and applications of GlobeLand30: A review," *ISPRS Int. J. Geo-Inf.*, vol. 6, no. 8, 2017, Art. no. 230.

[6] T. Esch *et al.*, "Breaking new ground in mapping human settlements from spacehe global urban footprint," *ISPRS J. Photogrammetry Remote Sens.*, vol. 134, pp. 30–42, 2017.

[7] P. Gong *et al.*, "Annual maps of global artificial impervious area (GAIA) between 1985 and 2018," *Remote Sens. Environ.*, vol. 236, 2020, Art. no. 111510. [Online]. Available: https://doi.org/10.1016/j.rse.2019.111510

[8] Q. Weng, "Remote sensing of impervious surfaces in the urban areas: Requirements, methods, and trends," *Remote Sens. Environ.*, vol. 117, pp. 34–49, 2012.

[9] L. Zhang, Q. Weng, and Z. Shao, "An evaluation of monthly impervious surface dynamics by fusing Landsat and MODIS time series in the Pearl River Delta, China, from 2000 to 2015," *Remote Sensing Environ.*, vol. 201, pp. 99–114, 2017.

[10] Y. Fu, *et al.*, "Mapping impervious surfaces in townrural transition belts using China's GF-2 imagery and object-based deep CNNs," *Remote Sens.*, vol. 11, no. 3, 2019, Art. no. 280.

[11] Y. Wang and M. Li, "Urban impervious surface detection from remote sensing images: A review of the methods and challenges," *IEEE Geosci. Remote Sens. Mag.*, vol. 7, no. 3, pp. 64–93, Sep. 2019.

[12] Y. Deng, R. Chen, and C. Wu, “Examining the deep belief network for subpixel unmixing with medium spatial resolution multispectral imagery in urban environments,” *Remote Sens.*, vol. 11, no. 13, 2019, Art. no. 1566.

[13] H. Xu, “Analysis of impervious surface and its impact on urban heat environment using the normalized difference impervious surface index (NDISI),” *Photogrammetric Eng.Remote Sens.*, vol. 76, no. 5, pp. 557–565, 2010.

[14] H. Zhang, Q. Weng, H. Lin, and Y. Zhang, *Remote Sensing of Impervious Surfaces in Tropical and Subtropical Areas*. Boca Raton, FL, USA: CRC Press, 2015.

[15] Y. Ban, A. Jacob, and P. Gamba, “Spaceborne SAR data for global urban mapping at 30 m resolution using a robust urban extractor,” *ISPRS J. Photogrammetry Remote Sens.*, vol. 103, pp. 28–37, May 2015. [Online]. Available: https://www.sciencedirect.com/science/article/abs/pii/S0924271614002032

[16] L. Yuan, Z. Yu, and W. Luo, “Towards the next-generation GIS: A geometric algebra approach,” *Ann. GIS*, vol. 25, no. 3 pp. 195–206, Jul. 2019. [Online]. Available: https://www.tandfonline.com/doi/full/10.1080/19475683.2019.1612945

[17] D. L. Niko, H. Hwang, Y. Lee, and C. Kim, *Integrating User-Generated Content and Spatial Data into Web GIS for Disaster History*. Heidelberg, Germany: Springer, 2011, pp. 245–255. [Online]. Available: http://link.springer.com/10.1007/978-3-642-21375-5_21

[18] J. Liang, S. Shen, J. Gong, J. Liu, and J. Zhang, “Embedding user-generated content into oblique airborne photogrammetry-based 3D city model,” *Int. J. Geographical Inf. Sci.*, vol. 31, no. 1 pp. 1–16, Jan. 2017. [Online]. Available: https://www.tandfonline.com/doi/full/10.1080/13658816.2016.1180389

[19] A. M. Kaplan and M. Haenlein, “Users of the world, unite! The challenges and opportunities of social media,” *Bus. Horizons*, vol. 53, no. 1 pp. 59–68, Jan. 2010. [Online]. Available: https://www.sciencedirect.com/science/article/pii/S0007681309001232

[20] F. Morstatter, H. Gao, and H. Liu, “Discovering location information in social media,” *IEEE Data Eng. Bull.*, vol. 38, no. 2 pp. 4–13, 2015. [Online]. Available: http://sites.computer.org/debull/A15june/p4.pdf

[21] F. Morstatter, J. Pfeffer, H. Liu, and K. M. Carley, “Is the sample good enough? Comparing data from Twitter’s streaming API with Twitter’s firehose,” in *Proc.17th Int. AAAI Conf. Weblogs Social Media*, 2013, pp. 400–408.

[22] D. Z. Sui, S. Elwood, and M. F. Goodchild, *Crowdsourcing Geographic Knowledge: Volunteered Geographic Information Theory and Practice*. New York, NY, USA: Springer, 2013.

[23] M. F. Goodchild, “Citizens as sensors: The world of volunteered geography,” *GeoJournal*, vol. 69, no. 4 pp. 211–221, Nov. 2007. [Online]. Available: http://link.springer.com/10.1007/s10708-007-9111-y

[24] D. Sui and M. Goodchild, “The convergence of GIS and social media: challenges for GIScience,” *Int. J. Geographical Inf. Sci.*, vol. 25, no. 11 pp. 1737–1748, Nov. 2011. [Online]. Available: http://www.tandfonline.com/doi/abs/10.1080/13658816.2011.604636

[25] J. Jokar Arsanjani, M. Helbich, M. Bakillah, and L. Loos, “The emergence and evolution of OpenStreetMap: A cellular automata approach,” *Int. J. Digit. Earth*, vol. 8, no. 1 pp. 76–90, Jan. 2015. [Online]. Available: http://www.tandfonline.com/doi/abs/10.1080/17538947.2013.847125

[26] Y. He, Y. Zheng, J. Deng, and H. Pan, “Design and implementation of a POI collection and management system based on public map service,” in *Proc. 4th Int. Conf. Ubiquitous Positioning, Indoor Navigation Location Based Services,* Nov. 2016, pp. 197–200. [Online]. Available: http://ieeexplore.ieee.org/document/7809971/

[27] X. Zhu and C. Zhou, “POI inquiries and data update based on LBS,” in *Proc. Int. Symp. Inf. Eng. Electron. Commerce*, 2009, pp. 730–734. [Online]. Available: http://ieeexplore.ieee.org/document/5175217/

[28] T. Ludwig, C. Kotthaus, C. Reuter, S. van Dongen, and V. Pipek, “Situated crowdsourcing during disasters: Managing the tasks of spontaneous volunteers through public displays,” *Int. J. Human-Comput. Stud.*, vol. 102, pp. 103–121, 2017. [Online]. Available: http://www.sciencedirect.com/science/article/pii/S1071581916301197

[29] N. Kankanamge, T. Yigitcanlar, A. Goonetilleke, and M. Kamruzzaman, “Can volunteer crowdsourcing reduce disaster risk? A systematic review of the literature,” *Int. J. Disaster Risk Reduction*, 2019. [Online]. Available: http://www.sciencedirect.com/science/article/pii/S2212420918310410

[30] P. S. Earle, D. C. Bowden, and M. Guy, “Twitter earthquake detection: Earthquake monitoring in a social world,” *Ann. Geophys.*, vol. 54, no. 6, pp. 708–715, 2012.

[31] M. T. Riccardi, “The power of crowdsourcing in disaster response operations,” *Int. J. Disaster Risk Reduction*, vol. 20, pp. 123–128, 2016. [Online]. Available: http://www.sciencedirect.com/science/article/pii/S2212420916302199

[32] Y. Liu, *et al.*, “Social sensing: A new approach to understanding our socioeconomic environments,” *Ann. Assoc. Amer. Geographers*, vol. 105, no. 3 pp. 512–530, May 2015. [Online]. Available: http://www.tandfonline.com/doi/full/10.1080/00045608.2015.1018773

[33] M. Madianou, “Humanitarian campaigns in social media,” *Journalism Stud.*, vol. 14, no. 2 pp. 249–266, Apr. 2013. [Online]. Available: http://www.tandfonline.com/doi/abs/10.1080/1461670X.2012.718558

[34] Y. Kryvasheyeu *et al.*, “Rapid assessment of disaster damage using social media activity,” *Sci. Adv.*, vol. 2, no. 3 Mar. 2016, Art. no. e1500779. [Online]. Available: http://advances.sciencemag.org/lookup/doi/10.1126/sciadv.1500779

[35] J. Li, Z. He *et al.*, “Social media: New perspectives to improve remote sensing for emergency response,” *Proc. IEEE*, vol. 105, no. 10, pp. 1900–1912, Oct. 2017.

[36] J. F. Rosser, D. G. Leibovici, and M. J. Jackson, “Rapid flood inundation mapping using social media, remote sensing and topographic data,” *Natural Hazards*, vol. 87, no. 1 pp. 103–120, May 2017. [Online]. Available: http://link.springer.com/10.1007/s11069-017-2755-0

[37] G. Panteras and G. Cervone, “Enhancing the temporal resolution of satellite-based flood extent generation using crowdsourced data for disaster monitoring,” *Int. J. Remote Sens.*, vol. 39, no. 5 pp. 1459–1474, Mar. 2018. [Online]. Available: https://www.tandfonline.com/doi/full/10.1080/01431161.2017.1400193

[38] R.-Q. Wang, H. Mao, Y. Wang, C. Rae, and W. Shaw, “Hyper-resolution monitoring of urban flooding with social media and crowdsourcing data,” *Comput. Geosci.*, vol. 111, pp. 139–147, Feb. 2018. [Online]. Available: https://www.sciencedirect.com/science/article/pii/S009830041730609X

[39] C. C. Fonte, L. Bastin, L. See, G. Foody, and F. Lupia, “Usability of VGI for validation of land cover maps,” *Int. J. Geographical Inf. Sci.*, vol. 29, no. 7 pp. 1269–1291, Jul. 2015. [Online]. Available: https://www.tandfonline.com/doi/full/10.1080/13658816.2015.1018266

[40] D. Hou *et al.*, “Active collection of land cover sample data from geo-tagged web texts,” *Remote Sens.*, vol. 7, no. 5 pp. 5805–5827, May 2015. [Online]. Available: http://www.mdpi.com/2072-4292/7/5/5805

[41] S. V. Stehman, C. C. Fonte, G. M. Foody, and L. See, “Using volunteered geographic information (VGI) in design-based statistical inference for area estimation and accuracy assessment of land cover,” *Remote Sens. Environ.*, vol. 212, pp. 47–59, Jun. 2018. [Online]. Available: https://www.sciencedirect.com/science/article/abs/pii/S0034425718301627

[42] H. Xing, Y. Meng, Z. Wang, K. Fan, and D. Hou, “Exploring geo-tagged photos for land cover validation with deep learning,” *ISPRS J. Photogrammetry Remote Sens.*, vol. 141, pp. 237–251, Jul. 2018. [Online]. Available: https://www.sciencedirect.com/science/article/abs/pii/S0924271618301333

[43] W. Su, D. Sui, and X. Zhang, “Satellite image analysis using crowdsourcing data for collaborative mapping: Current and opportunities,” *Int. J. Digit. Earth*, vol. 13, pp. 1–16, Dec. 2018. [Online]. Available: https://www.tandfonline.com/doi/full/10.1080/17538947.2018.1556352

[44] D. Ienco, K. Ose, and C. Weber, “Towards combining satellite imagery and VGI for urban LULC classification,” in *Proc. Joint Urban Remote Sens. Event*, May 2019, pp. 1–4. [Online]. Available: https://ieeexplore.ieee.org/document/8808966/

[45] P. Manandhar, P. R. Marpu, Z. Aung, and F. Melgani, “Towards automatic extraction and updating of VGI-based road networks using deep learning,” *Remote Sens.*, vol. 11, no. 9 Apr. 2019, Art. no. 1012. [Online]. Available: https://www.mdpi.com/2072-4292/11/9/1012

[46] Z. Miao *et al.*, “Integration of satellite images and open data for impervious surface classification,” *IEEE J. Sel. Topics Appl. Earth Observ. Remote Sens.*, vol. 12, no. 4 pp. 1120–1133, Apr. 2019. [Online]. Available: https://ieeexplore.ieee.org/document/8676248/

[47] H. Dorn, T. Törnros, and A. Zipf, “Quality evaluation of VGI using authoritative Data: A comparison with land use data in Southern Germany,” *ISPRS Int. J. Geo-Inf.*, vol. 4, no. 3 pp. 1657–1671, Sep. 2015. [Online]. Available: http://www.mdpi.com/2220-9964/4/3/1657

[48] J. Li, J. A. Benediktsson, B. Zhang, T. Yang, and A. Plaza, “Spatial technology and social media in remote sensing: A survey,” *Proc. IEEE*, vol. 105, no. 10, pp. 1855–1864, Oct. 2017.

[49] M. Jendryke, T. Balz, S. C. McClure, and M. Liao, “Putting people in the picture: Combining big location-based social media data and remote sensing imagery for enhanced contextual urban information in Shanghai,” *Comput., Environ. Urban Syst.*, vol. 62, pp. 99–112, Mar. 2017. [Online]. Available: https://www.sciencedirect.com/science/article/pii/S019897151630285X

[50] J.-F. Girres and G. Touya, “Quality assessment of the French OpenStreetMap dataset,” *Trans. GIS*, vol. 14, no. 4 pp. 435–459, Aug. 2010. [Online]. Available: http://doi.wiley.com/10.1111/j.1467-9671.2010.01203.x

[51] J. Yamashita, T. Seto, Y. Nishimura, and N. Iwasaki, “VGI contributors’ awareness of geographic information quality and its effect on data quality: A case study from Japan,” *Int. J. Cartography*, vol. 5, no. 2/3, pp. 214–224, May 2019. [Online]. Available: https://www.tandfonline.com/doi/full/10.1080/23729333.2019.1613086

[52] L. Zhang, M. Wang, W. Li, R. Hong, and M. Liu, “An automatic three-dimensional scene reconstruction system using crowdsourced geo-tagged videos,” *IEEE Trans. Ind. Electron.*, vol. 62, no. 9 pp. 5738–5746, Sep. 2015. [Online]. Available: http://ieeexplore.ieee.org/document/7056547/

[53] Y. Song, X. Chen, X. Wang, Y. Zhang, and J. Li, “6-DOF image localization from massive geo-tagged reference images,” *IEEE Trans. Multimedia*, vol. 18, no. 8 pp. 1542–1554, Aug. 2016. [Online]. Available: http://ieeexplore.ieee.org/document/7469851/

[54] L. Cheng *et al.*, “Crowd-sourced pictures geo-localization method based on street view images and 3D reconstruction,” *ISPRS J. Photogrammetry Remote Sens.*, vol. 141, pp. 72–85, Jul. 2018. [Online]. Available: https://www.sciencedirect.com/science/article/abs/pii/S0924271618301102

[55] W. Zhao, Y. Bo, J. Chen, D. Tiede, B. Thomas, and W. J. Emery, “Exploring semantic elements for urban scene recognition: Deep integration of high-resolution imagery and OpenStreetMap (OSM),” *ISPRS J. Photogrammetry Remote Sens.*, vol. 151, pp. 237–250, 2019.

[56] L. Qi, J. Li, Y. Wang, and X. Gao, “Urban observation: Integration of remote sensing and social media data,” *IEEE J. Sel. Topics Appl. Earth Observ. Remote Sens.*, vol. 12, no. 11 pp. 4252–4264, Nov. 2019. [Online]. Available: https://ieeexplore.ieee.org/document/8694019/

[57] Y. Qin, M. Chi, X. Liu, Y. Zhang, Y. Zeng, and Z. Zhao, “Classification of high resolution urban remote sensing images using deep networks by integration of social media photos,” in *Proc. IEEE Int. Geosci. Remote Sens. Symp.*, Jul. 2018, pp. 7243–7246. [Online]. Available: https://ieeexplore.ieee.org/document/8518538/

[58] H. Wang, E. Skau, H. Krim, and G. Cervone, “Fusing heterogeneous data: A case for remote sensing and social media,” *IEEE Trans. Geosci. Remote Sens.*, vol. 56, no. 12 pp. 6956–6968, Dec. 2018. [Online]. Available: https://ieeexplore.ieee.org/document/8412269/

[59] S. She, H. Zhong, Z. Fang, M. Zheng, and Y. Zhou, “Extracting flooded roads by fusing GPS trajectories and road network,” *ISPRS Int. J. Geo-Inf.*, vol. 8, no. 9, 2019, Art. no. 407.

[60] G. Lisini, A. Salentinig, P. Du, and P. Gamba, “SAR-based urban extents extraction: From ENVISAT to Sentinel-1,” *IEEE J. Sel. Topics Appl. Earth Observ. Remote Sens.*, vol. 11, no. 8, pp. 2683–2691, Aug. 2018.

[61] K. Heller, K. Svore, A. D. Keromytis, and S. Stolfo, “One class support vector machines for detecting anomalous windows registry accesses,” in *Proc. 3rd Int. Conf. Data Mining*, Melbourne, Florida, USA, 2003.

[62] J. Chen, Y. Wei, H. Wang, and X. Zhang, “Fault detection for turbine engine disk based on one-class large vector-angular region and margin,” *Math. Problems Eng.*, vol. 2020, 2020, Art. no. 5739345.

[63] X. Chen and D. Cai, “Large scale spectral clustering with landmark-based representation,” in *Proc. 25th AAAI Conf. Artifi. Intell.*, 2011, pp. 313–318.

[64] P. H. Seo, G. Kim, and B. Han, “Combinatorial inference against label noise,” in *Advances in Neural Information Processing Systems 32*, H. Wallach, H. Larochelle, A. Beygelzimer, F. d Alché-Buc, E. Fox, and R. Garnett, Eds. Red Hook, NY, USA: Curran Associates, Inc., 2019, pp. 1171–1181. [Online]. Available: http://papers.nips.cc/paper/8401-combinatorial-inference-against-label-noise.pdf

[65] M. Stasolla and P. Gamba, “Spatial indexes for the extraction of formal and informal human settlements from high-resolution SAR images,” *IEEE J. Sel. Topics Appl. Earth Observ. Remote Sens.*, vol. 1, no. 2, pp. 98–106, Jun. 2008.

Wen Wu received the B.S. degree in geographic information science from Central South University, Changsha, China, in 2017. She is currently working toward the M.Sc. degree with Central South University, Changsha, China.

Her research interests include image analysis, land cover, and the application of social media in remote sensing.

Zelang Miao (Member, IEEE) received the B.S. degree in surveying engineering and the M.S. degree in geodesy and surveying engineering from the China University of Mining and Technology, Xuzhou, China, in 2009 and 2014, respectively, and the Ph.D. degree in satellite image processing from The Hong Kong Polytechnic University, Hong Kong, in 2016.

He was a Visiting Ph.D. Student with the Department of Industrial and Information Engineering, University of Pavia, Pavia, Italy, in 2015. He is currently an Associate Professor with the School of Geoscience and Info-Physics, Central South University, Changsha, China. He has authored or co-authored over 30 papers on international and peer-reviewed scientific journals. His research interests include pattern recognition, land cover and land use mapping, and global/regional urbanization.

Dr. Miao serves as a Referee for IEEE Transactions on Geoscience and Remote Sensing, and IEEE Journal of Selected Topics in Remote Sensing Applications, Remote Sensing.

Yuelong Xiao received the B.S. degree in land source management from the Central South University of Forestry and Technology, Changsha, China, in 2017. He is currently working toward the M.Sc. degree with Central South University, Changsha, China.

His research interest includes monitoring environment of mineral areas using remote sensing.

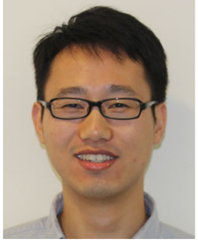

Zhongbin Li (Member, IEEE) received the B.Sc. degree in surveying engineering from Liaoning Technical University, Fuxin, China, in 2009, the M.Sc. degree in surveying engineering from Tongji University, Shanghai, China, in 2012, and the Ph.D. degree in remote sensing from The Hong Kong Polytechnic University, Hong Kong, in 2016.

In 2015, he was a Visiting Ph.D. Student with the School of Geographical Sciences and Urban Planning, Arizona State University, Tempe, AZ, USA. He is currently a Postdoctoral Research Fellow with the Geospatial Sciences Center of Excellence, South Dakota State University, Brookings, SD, USA. His research interests include remote sensing, land use and land cover change, and Landsat and Sentinel-2 data processing.

Dr. Li serves as a Reviewer for the *Remote Sensing of Environment* and the IEEE Transactions on Geoscience and Remote Sensing.

Anshu Zhang received the B.Sc. degree in geo-information technology and the Ph.D. degree in geographic information systems from The Hong Kong Polytechnic University, Hong Kong, in 2011 and 2017, respectively.

She is currently a Research Assistant Professor with the Department of Land Surveying and Geo-Informatics, The Hong Kong Polytechnic University. Her research interests include spatial data mining, human mobility modeling, and prediction, with the emphasis on improving the robustness and reliability of data analytics.

Dr. Zhang was the Secretary of Working Group II/1, The International Society for Photogrammetry and Remote Sensing from 2012 to 2016. She was the recipient of the China Science and Technology Progress Award in Surveying and Mapping (Grand Award) in 2017. She serves as a Referee of *International Journal of Geographical Information Science*, and *ACM Transactions on Data Science*.

Alim Samat (Member, IEEE) received the B.S degree in geographic information system from Nanjing University, Nanjing, China, in 2009, the M.E. degree in photogrammetry and remote sensing from China University of Mining and Technology, Xuzhou, China, in 2012, and the Ph.D. degree in cartography and geography information system from Nanjing University, Nanjing, China, in 2015.

He was a Visiting Ph.D. Student with the Department of Industrial and Information Engineering, University of Pavia, Pavia, Italy, in 2014. He is currently an Associate Professor with the State Key Laboratory of Desert and Oasis Ecology, Xinjiang Institute of Ecology and Geography, Chinese Academy of Sciences, Beijing, China. His main research interests include optical and PolSAR image processing and applications, machine learning, and pattern recognition.

Dr. Samat serves as a Reviewer for several international remote sensing journals, including *Remote Sensing Environment*, IEEE TRANSACTIONS ON GEOSCIENCE AND REMOTE SENSING, IEEE JOURNAL OF SELECTED TOPICS IN APPLIED EARTH OBSERVATION AND REMOTE SENSING, IEEE GEOSCIENCE AND REMOTE SENSING LETTERS, *ISPRS Journal of Photogrammetry and Remote Sensing*, *Remote Sensing*, *International Journal of Remote Sensing*, etc.

Nianchun Du received the B.Sc. degree in surveying engineering from Wuhan University, Wuhan, China, in 1991.

He is currently a Chief Engineer with China Nonferrous Metal Changsha Survey and Design Institute Company, Ltd., Changsha, China. He has a profound experience in integrated deformation monitoring system in the field of mining safety. His research interests include mine safety monitoring, natural hazard perception and cognition, and online monitoring system.

Mr. Du was the recipient of the China Science and Technology Progress Award in Surveying and Mapping, in 2012 and Hunan Science and Technology Progress Award, in 2012 and 2019, respectively.

Zhuokui Xu received the B.Sc. degree in surveying engineering, in 2001 from Henan Polytechnic University, Jiaozuo, China, the M.Sc. degree in cartography and geography information system, in 2005 from Wuhan University, Wuhan, China, and the Ph.D. degree in cartography and geographic information systems, in 2012 from Central South University, Changsha, China.

He is currently an Assistant Professor with the School of Traffic and Transportation Engineering, Changsha University of Science and Technology, Changsha, China. He has edited or co-edited four books. His research interests include web GIS, deformation monitoring, and engineering surveying.

Dr. Xu was the recipient of the China Science and Technology Progress Award in Surveying and Mapping, in 2006 and Hunan Science and Technology Progress Award, in 2012 and 2019, respectively.

Paolo Gamba (Fellow, IEEE) received the Laurea degree in electronic engineering cum laude, in 1989, and the Ph.D. degree in electronic engineering from the University of Pavia, Pavia, Italy, in 1993.

He is an Associate Professor of Telecommunications with the University of Pavia, where he also leads the Telecommunications and Remote Sensing Laboratory. He has been invited to give keynote lectures and tutorials in several occasions about urban remote sensing, data fusion, EO data, and risk management. He has authored or coauthored more than 110 papers in international peer-review journals and presented more than 250 research works in workshops and conferences.

Dr. Gamba served as the Editor-in-Chief of the IEEE GEOSCIENCE AND REMOTE SENSING LETTERS from 2009 to 2013, and as the Chair of the Data Fusion Committee of the IEEE Geoscience and Remote Sensing Society from October 2005 to May 2009. Currently, he is the Chair of the Chapters Committee of the same Society. He has been the organizer and Technical Chair of the biennial GRSS/ISPRS Joint Workshops on Remote Sensing and Data Fusion over Urban Areas, since 2001. He also served as the Technical Co-Chair of the 2010 IEEE Geoscience and Remote Sensing Symposium, Honolulu, Hawaii, July 2010 and Technical Co-Chair of the 2015 IEEE Geoscience and Remote Sensing Symposium, in Milan, Italy. He has been the Guest Editor of special issues of IEEE TRANSACTIONS ON GEOSCIENCE AND REMOTE SENSING, IEEE JOURNAL OF SELECTED TOPICS IN REMOTE SENSING APPLICATIONS, *ISPRS Journal of Photogrammetry and Remote Sensing*, *International Journal of Information Fusion*, and *Pattern Recognition Letters* on the topics of urban remote sensing, remote sensing for disaster management, pattern recognition in remote sensing applications.